Available online at www.sciencedirect.com
SCIENCE DIRECT®
International Journal of Solids and Structures 42 (2005) 1983–2009
INTERNATIONAL JOURNAL OF SOLIDS and STRUCTURES
www.elsevier.com/locate/ijsolstr

Element connectivity parameterization for topology optimization of geometrically nonlinear structures

Gil Ho Yoon, Yoon Young Kim *

Multiscale Design Center and Integrated Design and Analysis of Structures Laboratory, School of Mechanical and Aerospace Engineering, Kwanak-Gu Shinlim- Dong San 56-1, Seoul 151-742, Seoul National University, Seoul, Korea

Received 11 March 2004; received in revised form 15 September 2004
Available online 5 November 2004

Abstract

In the current element density-based topology optimization, element stiffness is penalized to yield either solid or void (or very weak) materials, but low-density elements appear during and even after optimization iterations. Especially when nonlinear problems involving large deformation are considered, low-density finite elements cause serious numerical problems as their tangent stiffness matrices lose positive definiteness. To completely eliminate the problem caused by low-density elements, we propose a new method: all finite elements are kept solid throughout the optimization process; zero-length elastic links are introduced to parameterize inter-element connectivity; the link stiffness is penalized. In this approach, the design variables are defined on the links, and vary from 0 and 1 corresponding to the unconnected and rigidly-connected states. Since the finite elements used to discretize the analysis domain always remain solid, typical numerical problems encountered by the standard element density-based formulation disappear. To implement the present method, several issues such as the handling of the mass constraint and raster imaging are also investigated.

Keywords: Topology optimization; Geometrically nonlinear problem; Element connectivity parameterization; Elastic link

1. Introduction

The topology optimization method originally formulated for linear structural problems has been expanded to various engineering problems. (Bendsøe and Kikuchi (1988), and Bendsøe and Sigmund

* Corresponding author. Tel.: +82 2 880 7130; fax: +82 2 883 1513.
E-mail address: yykim@snu.ac.kr (Y.Y. Kim).

0020-7683/$ - see front matter © 2004 Elsevier Ltd. All rights reserved.
doi:10.1016/j.ijsolstr.2004.09.005

(2003)) Nevertheless, some problems are still difficult to solve by the existing topology optimization formulation. The topology optimization of nonlinear structures, among others, is such a problem, so we aim to develop an efficient, effective method for the topology optimization of geometrically nonlinear structures.

When geometrically nonlinear structures discretized by finite elements have large deformation, low-stiffness elements can undergo excessive shape distortion and lose the positive definiteness of their tangent stiffness matrices. In this case, the corresponding finite elements are usually referred to as unstable elements. If this phenomenon occurs, many Newton–Raphson iterations are usually required and no converged solution may be found unless the convergence criterion is relaxed. When such poorly-converged solutions are used in an optimization, the optimization process usually slows down considerably while the objective function exhibits oscillatory behavior.

By noting that these numerical problems result mainly from low-stiffness elements which must be used within the current practice of topology optimization formulation, we aim at a new topology optimization formulation to completely eliminate such numerical problems, thus to avoid the occurrence of unstable elements due to the topology optimization formulation.

In the standard topology optimization formulation set up for both linear and nonlinear problems, the design variables varying continuously from 0 to 1 are assigned to all finite elements used to discretize a given design domain (see Bendsøe and Kikuchi, 1988; Bendsøe and Sigmund, 2003). To avoid intermediate densities and obtain black–white images, the element stiffness is then penalized, usually by the SIMP (Solid Isotropic Material with Penalization) method. Even if one can obtain an optimized design consisting mainly of void (or very week) and solid materials at the final iteration stage, low-density elements having low stiffness always appear during any topology design optimization process.

Low-density elements (corresponding to low-stiffness elements) alone do not cause serious numerical problems in linear static topology optimization problems, but they do in nonlinear topology optimization. If low-density elements, in particular, undergo extremely large deformation, the corresponding element tangent stiffness may become zero or negative, which leads to serious numerical instability problems (Gea and Luo, 2001; Bruns and Tortorelli, 2001; Bruns and Tortorelli, 2003; Pedersen et al., 2001; Buhl et al., 2000; Kobayashi et al., 1989; Belytschko et al., 2000; Cho and Jung, 2003).

To explain the numerical problem due to low-density elements, let us consider some numerical result in Fig. 1. Fig. 1(a) shows an optimized result, which one could obtain for a nonlinear compliance minimization problem by the convergence relaxation method (see Pedersen et al., 2001). In the standard element density-based formulation, void regions within the design boundary in Fig. 1(a) are actually filled with by very low-density finite elements. If one plots the deformation of the low-density elements near the loading point at a Newton-Raphson iteration (see Fig. 1(b)), one can immediately see the excessive distortions of such elements, which cause solution convergence problems. From a computational point of view, these low-

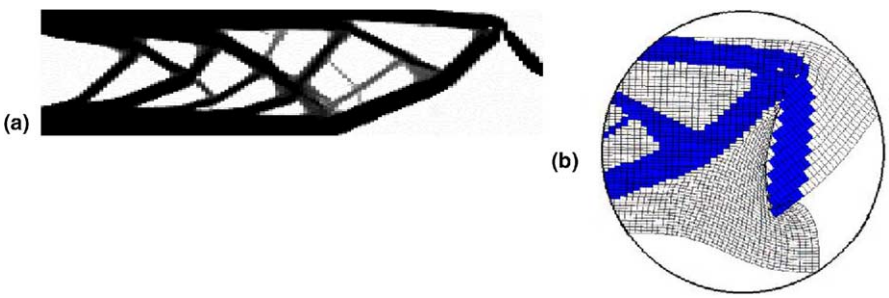

Fig. 1. The result for the end compliance problem using the method in Buhl et al. (2000) (a) a result (b) deformed shape during the Newton–Raphson iteration.

density finite elements lose the positive definiteness of their tangent stiffness matrices. We note here that the excessive distortions and numerical problems appearing in these elements are artificial problems that result from the current formulation practice of finite element density-based topology optimization.

Within the framework of the current finite element density-based formulation, several approaches, such as convergence relaxation during the Newton–Raphson iterations by Pedersen et al. (2001) and Buhl et al. (2000) and the element removal and reintroduction by Bruns and Tortorelli (2003), are developed to overcome the above-mentioned numerical problems. When the convergence relaxation strategy is used, the numerical instability problem is ignored, but the strategy still requires a large number of iterations and often yields incorrect or inaccurate results. Though the element density-based approach is used, the element removal and reintroduction method can handle the low-density element problems quite effectively.

Another interesting approach is the displacement-loading method by Cho and Jung (2003). The idea is to replace the force-loaded problem by an equivalent displacement-loaded problem, in which deformations even for low-density elements are small enough not to generate numerical instability. Cho and Jung (2003) presented an equivalent displacement-loading formulation, and verified its effectiveness through several case studies. However, it is difficult to apply it to general nonlinear force-loaded problems. For thorough reviews on low-density element problems, see Buhl et al. (2000) and Cho and Jung (2003).

From the above discussion, we see that low-density elements can cause numerical instability in most nonlinear problems. Because of the instability, we tried not use the densities of the finite elements as design variables, but kept all elements in solid state during the whole topology optimization process. Then, how do we find an optimal layout? Our idea is to assume that each finite element is connected to adjacent elements by artificial zero-length elastically deformable links at the interfacing nodes and to find optimal distribution of the elastic links; if the link stiffness is vanishingly small, then the corresponding node is regarded as being disconnected and if the link stiffness reaches a certain value, the corresponding node is regarded as being rigidly-connected. As in the standard formulation, the intermediate stiffness value can be avoided by penalization. In the SIMP approach, an element with an intermediate density may be interpreted as a certain micro structure. Since the present formulation works with a discretized model, the elastic links may be interpreted as some structural members connecting adjacent finite elements. Since the stiffness of the link varies, links having intermediate stiffness may be interpreted as one-dimensional linear elastic springs. In some engineering applications, elastic links were used to represent the actual system flexibility that cannot be correctly modeled by the employed finite element model (Chang, 1974; Kim et al., 1995).

It is emphasized again that the finite elements used to discretize the design domain remain solid during the whole topology optimization process, but only the stiffness of the artificial elastic links varies. Since the zero-length links have virtually no distortion problem even for large deformations, the numerical instability encountered in the standard formulation never appears. The price we must pay for this formulation is that the number of degrees of freedom for analysis increases by approximately four times in two-dimensional cases because of elastically linked finite elements. However, the present formulation actually takes much less computation time than the standard formulation, both in the Newton–Raphson iteration and in the optimization iteration.

For geometrically nonlinear topology optimization problems in consideration, we used the standard total Lagrangian formulation based on the Green–Lagrangian strain measure. To extract the optimal layout, the zero-length elastic links needed to be properly interpreted. Before applying the artificial zero-length elastic link method to nonlinear problems, we first checked its performance in linear problems. The effects of elastic link stiffness penalization on the optimized results were also examined. Since we employed displacement-based 4-node finite elements, the usual checkerboard problem also occured in the present formulation. We explained how to incorporate the filtering method in the present ECP approach. As numerical case studies, we considered benchmark nonlinear compliance minimization, compliant mechanism design, and multiphysics actuator problems.

2. Element connectivity parameterization (ECP)

Consider a finite element discretization of a design domain shown in Fig. 2. If SIMP (Solid Isotropic Material with Penalization) is used, each finite element has one design variable ρ_e which varies from a small number ε to 1.

In the SIMP formulation, the element stiffness $K_e(\rho_e)$ varies as

$$K_e(\rho_e) = \rho_e^n K_e^{\text{Solid}} \tag{1}$$

where K_e^{Solid} is the element stiffness when the original material property (i.e., $\rho_e = 1$) is used. The exponent n is the penalty factor. During topology optimization, elements having low density values or elements with artificially weak materials appear and these elements cause numerical difficulties when they undergo large deformation. Note that intermediate-density valued elements including low-density valued elements are artificial; these elements appear as the result of the converting void–solid discrete problems to continuous problems to facilitate the optimization process.

Since the appearance of low-density valued elements causes numerical difficulties in nonlinear analysis, we considered a new way of converting of void–solid discrete problems to continuous problem by using the element connectivity parameterization.

The key ideas of the proposed parameterization (see Fig. 3) are the followings:

(1) Analysis elements (two-dimensional plane elements in this case) are not used for design parameterization. These elements have the original material property throughout the whole design process.
(2) Artificial zero-length elastic links are introduced to determine the element connectivity, thus the layout of an optimal configuration. If the link stiffness becomes small or large, the adjacent elements are assumed to be disconnected or connected.
(3) By the use of a set of zero-length one dimensional elastic links, the plane elements can behave properly for (relatively) large displacement.

To compare the parameterizations by the existing element density SIMP method and the proposed method, we considered the modeling of a layout configuration by each method. As a typical layout configuration, we simply chose the one shown in Fig. 4(a) without the loss of generality.

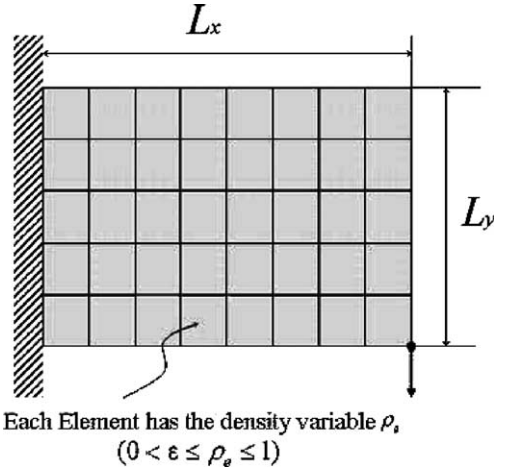

Fig. 2. The standard parameterization for topology optimization.

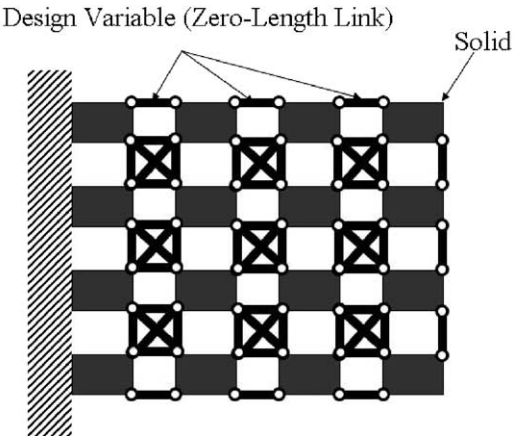

Fig. 3. The proposed design parameterization for topology optimization.

In the standard element density-based approach, the void region inside a prescribed design domain is modeled by plane finite elements having weak materials, i.e., low-density elements. In the proposed method, however, we modeled the layout in Fig. 4(a) by adjusting the stiffnesses of the zero-length elastic links connecting plane finite elements. Note that regardless of the layout pattern, the plane finite elements used to discretize the whole design domain remained to have the original material property. In the proposed ECP approach, the plane finite elements surrounded by low-stiffness elastic links represented void regions. Likewise, the plane finite elements connected by high-stiffness elastic links represented the desired layout. Therefore, the element connectivity was used to express solid or void regions. In this sense, the present formulation may be called the element connectivity-based topology optimization.

Now, we will explain in detail how the element connectivity was expressed by the link stiffness. Connections i in Fig. 5 represents the global node in the finite element discretization, but the terminology 'connection' will be used to emphasize that the element connectivity is the key concept in the present formulation.

Since the element connectivity will be designed to find an optimal layout, the design variables are assigned to the elastic links. Let γ^{pq} be the design variable assigned to the zero-length elastic link connecting nodes p and q at connection i (see Fig. 5). Since there are six possible link connections, (p,q) can take on (1,2), (1,3), (1,4), (2,3), (2,4), or (3,4). The design variable γ^{pq} takes on a value between γ_{LOW} and 1 as:

$$\gamma^{pq}_{\mathrm{LOW}} \leqslant \gamma^{pq} \leqslant \gamma^{pq}_{\mathrm{UPPER}} = 1 \tag{2}$$

where $\gamma^{pq}_{\mathrm{LOW}}$ is a small positive number (we use $\gamma_{\mathrm{LOW}} = 0.01$ in all problems). When γ^{pq} becomes 1, the nodes p and q are rigidly connected. On the other hand, when γ^{pq} becomes γ_{LOW}, the nodes p and q are regarded as being disconnected. To avoid intermediate element connections, we penalize the link stiffness l^{pq}_i as

$$l^{pq}_i = l_0(\gamma^{pq}_i)^n \tag{3}$$

where l_0 is the upper bound of the elastic link simulating the rigid connection and n is the penalty exponent that plays exactly the same role as that used in the SIMP approach. The theoretical value of the upper bound l_0 must approach infinity. Some care must be taken in choosing the value of l_0. This issue will be discussed later, so we simply state here that the value of l_0 used in this work is approximately 10 to 10^4 times larger than the diagonal stiffness element of the adjacent plane element.

Since each link has the four degrees of freedom in plane problems (see Fig. 6), the link element stiffness k^{link}_e can be defined as

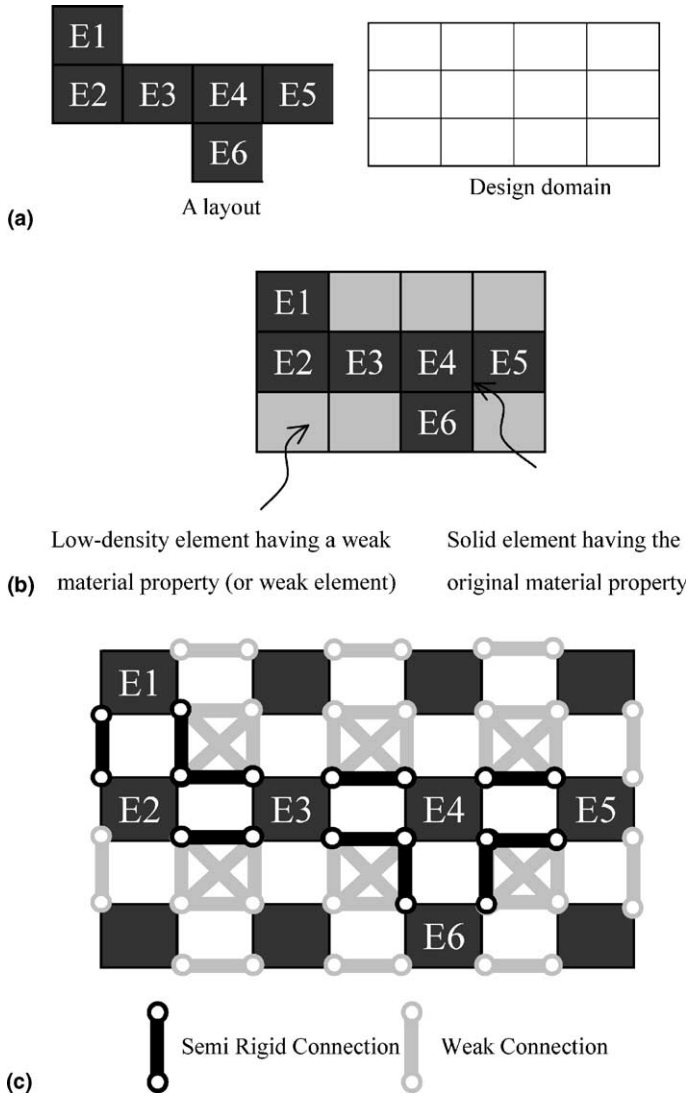

Fig. 4. Layout modeling: (a) a typical layout needed during topology optimization, (b) the layout modeled by the existing element density-based SIMP method, and (c) the layout modeled by the proposed zero-length elastic link method.

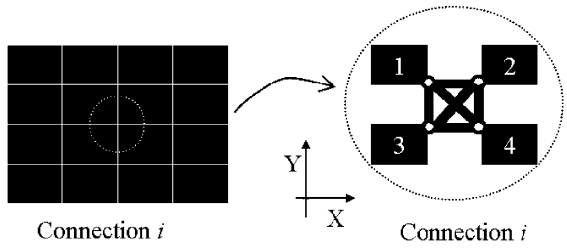

Fig. 5. Element connectivity by zero-length one-dimensional elastic links at connection *i*.

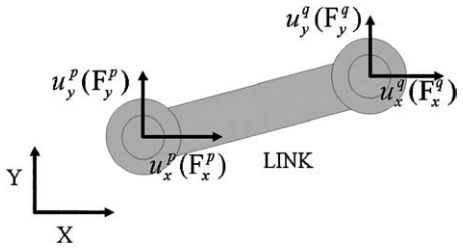

Fig. 6. Link element connecting nodes p and q at connection i.

$$k^{\text{link}}_{i,(pq)} = l_i^{pq} k^{\text{link}}_{\text{nominal}} = l_i^{pq} \begin{bmatrix} 1 & 0 & -1 & 0 \\ 0 & 1 & 0 & -1 \\ -1 & 0 & 1 & 0 \\ 0 & -1 & 0 & 1 \end{bmatrix} \tag{4a}$$

$$\begin{bmatrix} F_x^p \\ F_y^p \\ F_x^q \\ F_y^q \end{bmatrix} = k^{\text{link}}_{i,(pq)} \begin{bmatrix} u_x^p \\ u_y^p \\ u_x^q \\ u_y^q \end{bmatrix} \tag{4b}$$

where u and F denote the nodal displacement and the nodal force, respectively, and the subscripts x and y denote the coordinate directions. In Eq. (4a), the link element is assumed to have the same stiffness in the x and y directions.

Referring to Fig. 6, we introduced six independent link elements (thus six design variables) at each connection, such as $k^{\text{link}}_{i,(12)}$, $k^{\text{link}}_{i,(13)}$, $k^{\text{link}}_{i,(14)}$, $k^{\text{link}}_{i,(23)}$, $k^{\text{link}}_{i,(24)}$, $k^{\text{link}}_{i,(34)}$. This modeling will be referred to as 6-DV link modeling. On the other hand, one may introduce only one design variable γ_i by imposing that

$$\gamma_i \equiv \gamma_i^{12} = \gamma_i^{13} = \gamma_i^{14} = \gamma_i^{23} = \gamma_i^{24} = \gamma_i^{34} \tag{5}$$

This modeling, which is referred to as 1-DV link modeling, reduces the number of design variables and avoids strip-like link distribution as shall be seen later. We will compare the optimized results between the 6-DV link modeling and the 1-DV link modeling, but we will mainly use the 1-DV link modeling approach. [1]

2.1. Representation of optimized results by the ECP approach

Since the link is given no length for the sake of accurate structural analysis, it may be difficult to plot the optimal structural layout corresponding to a given distribution of the design values γ_i (or γ_i^{pq}). Here, we propose a raster imaging scheme to find the structural layout configuration from the given distribution of γ_i. To explain the raster imaging scheme, let us consider a distribution of γ_i in Fig. 7(a). In Fig. 7(a), the values of

[1] When the 1-DV link modeling technique is used, the link assembly exhibits isotropic behavior (Suzuki, 2003), but the 6-DV link assembly does not.

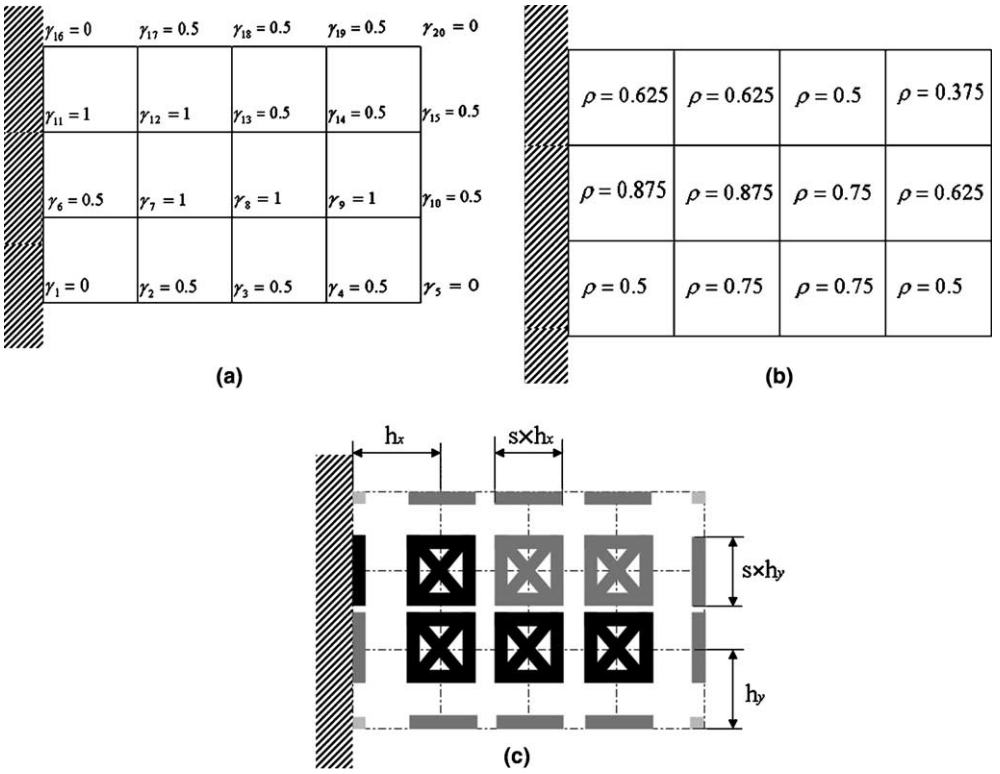

Fig. 7. Skeleton and raster imaging schemes or a given distribution of the link design variables γ_i (a) distribution of γ_i, (b) raster imaging scheme by Eq. (6), and (c) skeleton imaging scheme (gray levels correspond to the values of γ_i).

γ_i corresponding to the 1-DV modeling technique are listed, but the raster imaging scheme equally applies to the 6-DV modeling technique.

The raster imaging scheme is demonstrated in Fig. 7(b). In this scheme, the values of the link design variables γ_i are distributed to adjacent plane finite elements by simple averaging. Since a finite element is surrounded by four links defined at its nodes (see Fig. 7), one may assign an element density ρ_e as

$$\rho_e = \frac{1}{4}(\gamma_1 + \gamma_2 + \gamma_3 + \gamma_4), \quad (0 \leqslant \rho_e \leqslant 1) \tag{6}$$

To see the rationale behind Eq. (6), we make the following observations. When all γ_i $(i = 1,2,3,4)$ reach the upper bound $\gamma_{\mathrm{UPPER}} = 1$, the element surrounded by these links behaves as a solid element as predicted by Eq. (6). On the other hand, the element surrounded by links with $\gamma_i = \gamma_{\mathrm{LOW}}$ $(i = 1,2,3,4)$ will behave as a void element. Likewise, intermediate values of γ_i surrounding a plane finite element can be properly interpreted by Eq. (6). It is worth emphasizing that the transformation between γ_i and ρ_e is used only for imaging purpose and the plane elements remain solid ($\rho_e = 1$) throughout all optimization iterations.

It will be also interesting to plot γ_i directly at the ith connection. For effective visualization of γ_i, the link may be treated to have finite lengths $(s \times h_x, s \times h_y)$ $(s \in [0,1])$ where h_x and h_y are the horizontal and vertical lengths of the adjacent element. If $s = 1$ is used, one may easily visualize the skeleton of the optimized structure. Although this representation, which will be called the skeleton imaging representation, is not the primary method to represent the final result, it may be interesting to see the skeleton image as shown in Fig. 7(c).

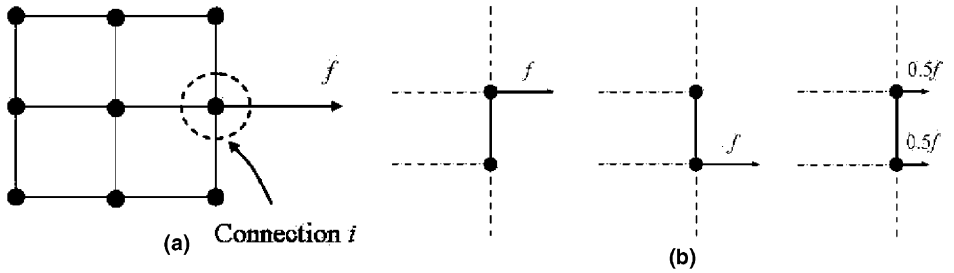

Fig. 8. Load distributions of a point force in the present link-based formulations: (a) load applied at connection i, (b) three typical load distributions when links are introduced.

2.2. Handling of applied loads and mass constraints

In the proposed approach, plane finite elements are connected by elastic links. Therefore, some considerations on point loading may be necessary.

Within the proposed link-based formulation, three typical load distributions illustrated in Fig. 8(b) can be used. However, the optimized results were virtually independent of the load distribution methods.

Mass constraint handling should also be considered. The design variables are defined on artificial zero-length elastic links, but the design variables themselves are not directly related to the mass of the solid part of a design domain. Based on the rationale used for the raster imaging scheme, however, one can define the density of the plane finite element by Eq. (6). Again, the relation between ρ_e and γ_i is used for the mass evaluations, not for analysis.

3. Verification of the proposed method in linear problems

Before applying the proposed element connectivity parameterization method by zero-length elastic links, we consider applying the ECP method to linear problems. The main motivation to consider is to convey the proposed idea more easily and to check its validity for the fundamental linear problem. As a case study, we will use the classical linear compliance minimization problem. For comparison with the present formulation, we state briefly the standard SIMP-based topology optimization formulation for the compliance minimization problem.

$$\underset{\boldsymbol{\rho}}{\text{Min}} \quad W(\boldsymbol{\rho}) = \mathbf{F}^{\mathrm{T}}\mathbf{U}(\boldsymbol{\rho}) = \mathbf{U}(\boldsymbol{\rho})^{\mathrm{T}}\mathbf{K}(\boldsymbol{\rho})\mathbf{U}(\boldsymbol{\rho}) \tag{7a}$$

$$\text{subject to} \quad \sum_{e=1}^{N_p} \rho_e v_e \leqslant V^* \quad (V^* : \text{prescribed volume}) \tag{7b}$$

where $\mathbf{U}$ is the nodal displacement while $\mathbf{F}$ is the nodal load. The global stiffness matrix $\mathbf{K}$ is assembled as $\mathbf{K} = \sum_{e=1}^{N_p} k_e(\rho_e)$ where the element stiffness matrix k_e in the standard approach is a function of the element density ρ_e as

$$k_e(\rho_e) = \int_{v_e} B^{\mathrm{T}} C(\rho_e) B \, \mathrm{d}V_e$$

The matrix B relates the nodal displacement and the strain, which can be found in standard text books on the finite element method. In the SIMP method, the constitutive matrix C is a penalized function of ρ_e (see Bendsøe and Sigmund, 2003).

Now we will state how the compliance minimization problem is formulated by the present element connectivity parameterization method.

$$\underset{\gamma}{\text{Min}} \quad W(\boldsymbol{\gamma}) = \mathbf{F}^{\mathrm{T}}\mathbf{U}(\boldsymbol{\gamma}) = \mathbf{U}(\boldsymbol{\gamma})^{\mathrm{T}}\mathbf{K}(\boldsymbol{\gamma})\mathbf{U}(\boldsymbol{\gamma}) \tag{8}$$

$$\text{subject to} \quad \sum_{e=1}^{N_P} \rho_e(\boldsymbol{\gamma}) v_e \leqslant V^* \tag{9}$$

In the present formulation, the stiffness matrix $\mathbf{K}(\boldsymbol{\gamma})$ consists of two parts as

$$\mathbf{K} = \mathbf{K}^{\text{structure}} + \mathbf{K}^{\text{link}}(\boldsymbol{\gamma}) \tag{10}$$

In Eq. (10), $\mathbf{K}^{\text{structure}}$ is the stiffness matrix obtained by the plane finite element discretization and is independent of the design variable $\boldsymbol{\gamma}$. The matrix $\mathbf{K}^{\text{link}}(\boldsymbol{\gamma})$ is the stiffness matrix resulting from the presence of zero-length elastic links and is the function of the design variable $\boldsymbol{\gamma}$. It is noted that for the same finite element discretization used to solve Eqs. (7) and (8), the size of $\mathbf{U}(\boldsymbol{\gamma})$ in Eq. (8) is approximately four times larger than the size of $\mathbf{U}(\boldsymbol{\rho})$ in Eq. (7). This is because four nodes at every connection have different degrees of freedom.

The global matrices $\mathbf{K}^{\text{structure}}$ and $\mathbf{K}^{\text{link}}$ are simply assembled by means of element stiffness matrices $k_e^{\text{structure}}$ and $k_e^{\text{link}}(\gamma_e)$ as

$$\mathbf{K}^{\text{structure}} = \sum_{e=1}^{N_p} k_e^{\text{structure}} \quad \text{(independent of } \boldsymbol{\gamma}\text{)} \tag{11a}$$

$$\mathbf{K}^{\text{link}} = \sum_{i=1}^{N_e} k_i^{\text{link}} = \sum_{i=1}^{N_e} l_0(\gamma_i)^n k_{\text{nominal}}^{\text{link}} \tag{11b}$$

where N_e is the total number of zero-length links.

The sensitivity of the compliance $W(\boldsymbol{\gamma})$ with respect to γ_i can be computed simply as

$$\frac{\partial W}{\partial \gamma_i} = -\mathbf{U}^{\mathrm{T}} \frac{\partial \mathbf{K}^{\text{link}}}{\partial \gamma_i}\mathbf{U} = -u_i^{\mathrm{T}} \frac{\mathrm{d}k_i^{\text{link}}}{\mathrm{d}\gamma_i} u_i = -\frac{n}{\gamma_i} u_i^{\mathrm{T}} k_i^{\text{link}} u_i \tag{12}$$

where the equilibrium condition $\mathbf{KU} = \mathbf{F}$ is used to obtain the first expression in Eq. (11). As in the element density-based method, the sensitivity of $W(\boldsymbol{\gamma})$ with respect to the ith design variable is written only in terms of the nodal displacement vector u_i (having eight degrees of freedom at connection i of Fig. 5) and the stiffness matrix k_i^{link}. In fact, Eq. (12) shows how the strain energy ($u_i^{\mathrm{T}} k_i^{\text{link}} u_i$) of the link at connection i is related to the sensitivity $\partial W/\partial \gamma_i$.

To check the performance of the proposed element connectivity parameterization, we will consider the compliance minimization problem depicted in Fig. 2. For this problem, linear stress and strain measures are used. The numerical data used are as follows: $L_x = 60$, $L_y = 30$, $F = 1$, Young's modulus $E = 1$, Poisson's ratio $v = 0.3$, mass constraint ratio = 30%. For the analysis, the design domain is discretized by 60×30 by four-node bilinear plane finite elements and the elements are then assumed to be connected by elastic links for the present topology optimization formulation.

Fig. 9 shows the optimized result based on the present element connectivity parameterization method using zero-length elastic links. Both skeleton and raster images are shown in Fig. 9. The result by the 6-DV link modeling exhibits strip-like link connectivity and the resulting raster image is somewhat blurred. These strip-like patterns may give the designer some insight, but we have also employed a simpler 1-DV link modeling approach to obtain better images and to reduce the number of the design variables. In the future,

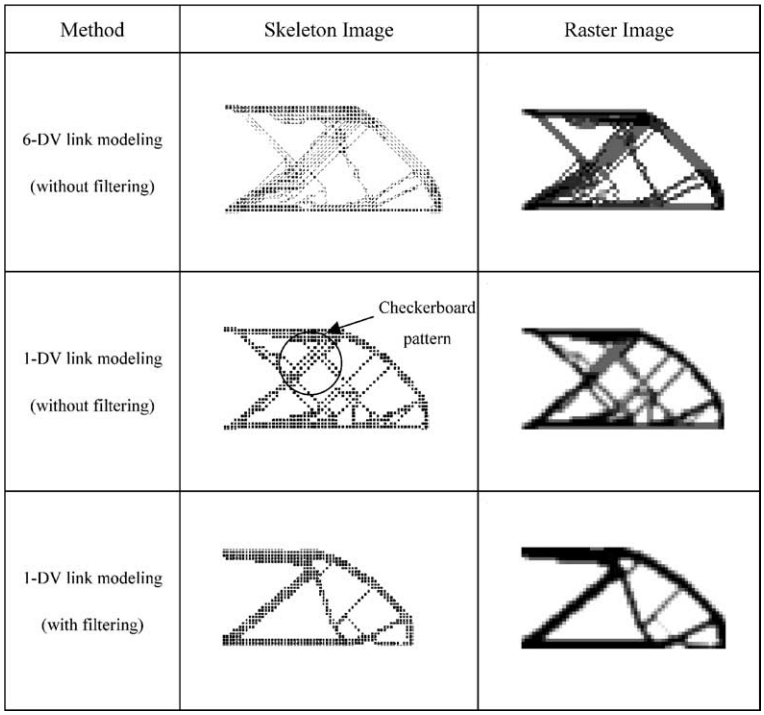

Fig. 9. The optimized results by the proposed element connectivity parameterization method for the Michell compliance minimization problem.

more investigations of the 6-DV link modeling may find its effectiveness in some applications, but we will mainly work with the 1-DV link modeling technique throughout this work.

Because four-node displacement bilinear finite elements are employed for analysis (see, Sigmund and Petersson, 1998), the well-known checkerboard patterns are also formed in the present ECP method. To avoid the checkerboard formation, the filter used for the standard element density method is extended for the ECP formulation (see, Sigmund and Petersson, 1998). Specifically, the sensitivity is averaged as

$$\frac{\mathrm{d}\overline{W}}{\mathrm{d}\gamma_C} = \left(\frac{\mathrm{d}W}{\mathrm{d}\gamma_C} + \frac{\mathrm{d}W}{\mathrm{d}\gamma_L} + \frac{\mathrm{d}W}{\mathrm{d}\gamma_R} + \frac{\mathrm{d}W}{\mathrm{d}\gamma_U} + \frac{\mathrm{d}W}{\mathrm{d}\gamma_B}\right) \Big/ 5 \tag{13}$$

where the meaning of the symbols C, L, R, U, and B can be found in Fig. 10. Modified versions of Eq. (13) may be used, but Eq. (13) will be used in this work. Obviously, filtering tends to produce larger grey regions associated with intermediate design variables.

Though the penalty exponent used in Eq. (3) to penalize the link stiffness is expected to have the same effect as in the SIMP approach, it is worth examining the effect of the exponent on the optimized result. Fig. 11 illustrates how the optimized results change as the exponent n increases. This figure shows that the role of the penalty exponent in the present ECP approach is identical to that in the SIMP method.

Now we investigate the effect of the upper bound l_0 of the elastic link on the solution. In selecting the value of l_0, we note that $l_0 \times {\gamma_{\mathrm{UPPER}}}^n$ ($\gamma_{\mathrm{UPPER}} = 1$) should be sufficiently large to simulate the rigid connection between the nodes connected by a given link but moderately large so as not to cause any numerical problem. At the same time, the link stiffness value of $l_0 \times {\gamma_{\mathrm{LOW}}}^n$ ($\gamma_{\mathrm{LOW}} = 0.01$) should be sufficient small enough to simulate no connection between the nodes connected by a given link, but moderately small so

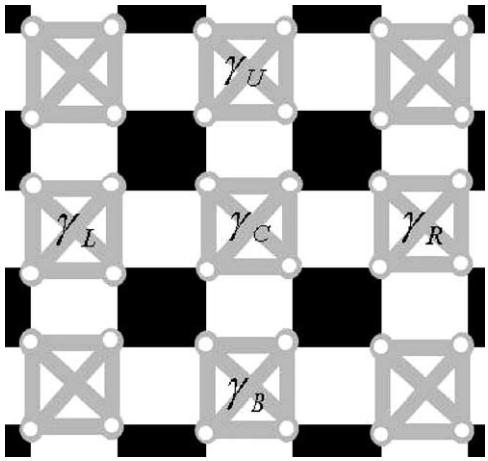

Fig. 10. The used filter for the sensitivity.

Penalty exponent n	Skeleton Images	Raster Images
n =2		
n =5		
n =6		

Fig. 11. The effects of the link stiffness penalty exponent.

Upper bound of link stiffness	Skeleton Image	Raster Image
l_0=100		
l_0=1.0×10^4		
l_0=1.03×10^5		

Fig. 12. The effects of the value of the link stiffness upper bound l_0 on the optimized solution (In this case, the penalty exponent $n = 4$, the value of the diagonal stiffness of the plane finite element=0.494.).

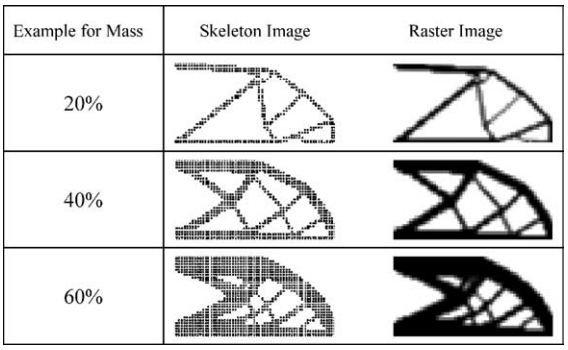

Fig. 13. The behavior of the optimized designs for varying mass constraint ratios.

as not to cause any singularity. Therefore, the choice of l_0 is independent of the value of n. Several numerical tests have indicated that relatively large values of n around 4 work satisfactorily and the effects of l_0 for $n = 4$ are shown in Fig. 12.

If the upper bound l_0 takes on a very large value, $l_0 \times \gamma_{\mathrm{LOW}}{}^n$ increases and thus grey areas become larger in the raster image. Therefore, the value of l_0 should be moderately large as in the second case of Fig. 12. To penalize the last example of Fig. 12, we may adopt a higher penalization n, or a continuation method for n.

Finally, we have also checked if the mass constraints were correctly reflected in the optimized result obtained by the present element connectivity parameterization formulation. As shown in Fig. 13, the increase in the mass constraint ratio was well reflected in the optimized result, which validated the present mass evaluation scheme stated as Eq. (6).

4. Nonlinear analysis using the link modeling technique

Before solving topology optimization problems for geometrically nonlinear structures, we will consider how effective the present link modeling technique is in solving the geometrically nonlinear response of a structure consisting of strong and weak materials. This structure may be viewed as a typical layout appearing at intermediate stages during topology optimization process.

We will begin with a brief summary of the total Lagrangian formulation for geometrical nonlinear analysis and explain how the formulation is changed if the proposed link modeling technique is introduced. To show the superior performance of the proposed link modeling technique, we will analyze a geometrical nonlinear structure.

4.1. Underlying nonlinear analysis and the link modeling technique

For geometric nonlinear analysis, we will use the total Lagrangian (TL) formulation using the second Piola–Kirchoff stress and the Green–Lagrangian strain. The TL formulation for geometric nonlinear analysis is well established, and it is useful to write the key equations for later use. The notation and formulation given in Bathe (1996) will be used in this work.

By denoting the coordinates and displacements of a generic point in a body by x_i and u_i $(i = 1, 2, 3)$, we can write the following relations

$$ {}^{t}x_i = {}^{0}x_i + {}^{t}u_i, \quad {}^{t+\Delta t}u_i = {}^{t}u_i + u_i \tag{14}$$

In Eq. (14), the left superscripts t, $t + \Delta t$, 0 stand for the time at which the body is observed.

In total incremental Lagrangian formulation, the principle of the virtual work at time $t+\Delta t$ can be written as

$$ {}_0^{t+\Delta t}\mathbf{F} = {}^{t+\Delta t}\mathbf{R} \tag{15a} $$

$$ {}_0^{t+\Delta t}\mathbf{F} = \int_{{}_0V} {}_0^{t+\Delta t}S_{ij}\delta_0{}^{t+\Delta t}\epsilon_{ij}\,\mathrm{d}^0V \tag{15b} $$

$$ {}^{t+\Delta t}\mathbf{R} = \int_{{}_0V} {}^{t+\Delta t}f_i^B\delta u_i\,\mathrm{d}^0V + \int_{{}_0S_f} {}^{t+\Delta t}f_i^S\delta u_i^S\,\mathrm{d}^0S \tag{15c} $$

where ${}_0^{t+\Delta t}S_{ij}$ is the second Piola–Kirchhoff stress and ${}_0^{t+\Delta t}\epsilon_{ij}$ is the Green–Lagrangian strain defined as

$$ {}_0^{t+\Delta t}e_{ij} = \frac{1}{2}\left(\frac{\partial^{t+\Delta t}u_i}{\partial^0 x_j} + \frac{\partial^{t+\Delta t}u_j}{\partial^0 x_i} + \frac{\partial^{t+\Delta t}u_k}{\partial^0 x_i}\frac{\partial^{t+\Delta t}u_k}{\partial^0 x_j}\right) \tag{16} $$

The left subscript 0 implies that the quantities of interest are measured with respect to the initial configuration at time 0. In Eq. (15), ${}^{t+\Delta t}f_i^{\mathrm{B}}$ and ${}^{t+\Delta t}f_i^{\mathrm{S}}$ denote the body force and the surface traction at time $t+\Delta t$, respectively. The virtual quantities in Eq. (15) are expressed with the symbol δ.

In geometric nonlinear analysis, assuming large displacements but small strains, the equilibrium equation must be expressed in nonlinear form, equivalently in the incremental form as Eq. (15), but a linear constitutive relation may be used:

$$ {}_0^{t+\Delta t}S_{ij} = C_{ijkl}{}_0^{t+\Delta t}\epsilon_{kl} \tag{17} $$

Substituting Eq. (17) into Eq. (15) with the following update rules,

$$ {}_0^{t+\Delta t}S_{ij} = {}_0^{t}S_{ij} + {}_0S_{ij} \tag{18} $$

$$ {}_0^{t+\Delta t}\epsilon_{ij} = {}_0^{t}\epsilon_{ij} + {}_0\epsilon_{ij} \tag{19} $$

where

$$ {}_0\epsilon_{ij} = {}_0e_{ij} + {}_0\eta_{ij} \tag{20} $$

$$ {}_0e_{ij} = \frac{1}{2}({}_0u_{i,j} + {}_0u_{j,i} + {}_0^{t}u_{k,i0}u_{k,j} + {}_0u_{k,i0}{}_0^{t}u_{k,j}) \tag{21} $$

$$ {}_0\eta_{ij} = \frac{1}{2}({}_0^{t}u_{k,i0}u_{k,j}) \tag{22} $$

one can obtain the linearized form of Eq. (15) as

$$ \int_{{}_0V} C_{ijrs}{}_0e_{rs}\delta_0e_{ij}\,\mathrm{d}^0V + \int_{{}_0V} {}_0^{t}S_{ij}\delta_0\eta_{ij}\,\mathrm{d}^0V = {}^{t+\Delta t}R - \int_{{}_0V} {}_0^{t}S_{ij}\delta_0e_{ij}\,\mathrm{d}^0V \tag{23} $$

Note that the incremental stress and strain are denote by ${}_0S_{ij}$ and ${}_0\epsilon_{ij}$ and that ${}_0\epsilon_{ij}$ is divided into the linear part ${}_0\eta_{ij}$, and the nonlinear part ${}_0e_{ij}$. The incremental displacement from ${}^{t}u_i$ to ${}^{t+\Delta t}u_i$ is denoted by ${}_0u_i$ in Eqs. (21) and (22). Since ${}_0u_i$ (and ${}_0S_{ij}$ and ${}_0\epsilon_{ij}$) cannot be determined explicitly because of the nonlinearity involved, the Newton–Raphson iterative scheme will be used for numerical implementation of Eq. (23).

If the iteration step of the Newton–Raphson method is denoted by k, the displacement is updated as

$$ {}^{t+\Delta t}u_i^{(k)} = {}^{t+\Delta t}u_i^{(k-1)} + \Delta u_i^{(k)} \tag{24} $$

with

$$ {}^{t+\Delta t}u_i^{(0)} = {}^{t}u_i \tag{25} $$

If the displacement field is approximated according to the standard displacement-based finite element method, one may obtain the following system of equations for the nodal displacement $\Delta\mathbf{U}^{(k)}$ corresponding to $\Delta u_i^{(k)}$:

$$\left({}_0^t\mathbf{K}_{\mathrm{L}}^{(k-1)} + {}_0^t\mathbf{K}_{\mathrm{NL}}^{(k-1)}\right)\Delta\mathbf{U}^{(k)} = {}^{t+\Delta t}\mathbf{R} - {}_0^{t+\Delta t}\mathbf{F}^{(k-1)} \tag{26a}$$

$${}^{t+\Delta t}\mathbf{U}^{(k)} = {}^{t+\Delta t}\mathbf{U}^{(k-1)} + \Delta\mathbf{U}^{(k)} \tag{26b}$$

$${}_0^t\mathbf{K}_{\mathrm{L}}^{(k-1)} = \int_{{}_0V}\left({}_0^t\mathbf{B}_{\mathrm{L}}^{(k-1)}\right)^{\mathrm{T}}\mathbf{C}_0\,{}_0^t\mathbf{B}_{\mathrm{L}}^{(k-1)}\,\mathrm{d}^0V \tag{26c}$$

$${}_0^t\mathbf{K}_{\mathrm{NL}}^{(k-1)} = \int_{{}_0V}\left({}_0^t\mathbf{B}_{\mathrm{NL}}^{(k-1)}\right)^{\mathrm{T}}{}_0^t\mathbf{S}^{(k-1)}\,{}_0^t\mathbf{B}_{\mathrm{NL}}^{(k-1)}\,\mathrm{d}^0V \tag{26d}$$

$${}_0^{t+\Delta t}\mathbf{F}^{(k-1)} = \int_{{}_0V}\left({}_0^{t+\Delta t}\mathbf{B}_{L}^{(k-1)}\right)^{\mathrm{T}}{}_0^{t+\Delta t}\widehat{\mathbf{S}}^{(k-1)}\,\mathrm{d}^0V \tag{26e}$$

$${}_0^{t+\Delta t}\mathbf{S}^{(k-1)} = \begin{bmatrix} {}_0^{t+\Delta t}S_{11}^{(k-1)} & {}_0^{t+\Delta t}S_{12}^{(k-1)} & {}_0^{t+\Delta t}S_{13}^{(k-1)} & 0 & 0 & 0 \\ {}_0^{t+\Delta t}S_{21}^{(k-1)} & {}_0^{t+\Delta t}S_{22}^{(k-1)} & {}_0^{t+\Delta t}S_{23}^{(k-1)} & 0 & 0 & 0 \\ {}_0^{t+\Delta t}S_{31}^{(k-1)} & {}_0^{t+\Delta t}S_{32}^{(k-1)} & {}_0^{t+\Delta t}S_{33}^{(k-1)} & 0 & 0 & 0 \\ 0 & 0 & 0 & {}_0^{t+\Delta t}S_{11}^{(k-1)} & {}_0^{t+\Delta t}S_{12}^{(k-1)} & {}_0^{t+\Delta t}S_{13}^{(k-1)} \\ 0 & 0 & 0 & {}_0^{t+\Delta t}S_{21}^{(k-1)} & {}_0^{t+\Delta t}S_{22}^{(k-1)} & {}_0^{t+\Delta t}S_{23}^{(k-1)} \\ 0 & 0 & 0 & {}_0^{t+\Delta t}S_{31}^{(k-1)} & {}_0^{t+\Delta t}S_{32}^{(k-1)} & {}_0^{t+\Delta t}S_{33}^{(k-1)} \end{bmatrix} \tag{26f}$$

$${}_0^{t+\Delta t}\widehat{\mathbf{S}}^{(k-1)} = \left[{}_0^{t+\Delta t}S_{11}^{(k-1)}, {}_0^{t+\Delta t}S_{22}^{(k-1)}, {}_0^{t+\Delta t}S_{33}^{(k-1)}, {}_0^{t+\Delta t}S_{12}^{(k-1)}, {}_0^{t+\Delta t}S_{23}^{(k-1)}, {}_0^{t+\Delta t}S_{31}^{(k-1)}\right] \tag{26g}$$

$$\mathscr{R}^k = \Delta\mathbf{U}^{(k)}, \quad \|\mathfrak{R}^{(k)}\| \leqslant \varepsilon_{\mathrm{NR}} \tag{26h}$$

In Eq. (26), the matrices ${}_0^{t+\Delta t}B_{\mathrm{L}}$ and ${}_0^{t+\Delta t}B_{\mathrm{NL}}$ represent the strain–displacement transformation matrices, and L and NL stand for linear and nonlinear cases. In the present formulation, we use 4-node bilinear plane elements for displacement field approximation. The matrix $\mathbf{C}_0$ denotes the matrix form of the constitutive relation constructed from c_{ijkl}. When the residual $\mathfrak{R}^{(k)}$ satisfies the condition in Eq. (26h), the final displacement $\widehat{\mathbf{U}}$ for a given load is obtained. See Bathe (1996) for more details on the finite element formulation of geometrical nonlinear analysis.

When the proposed link modeling technique is introduced to the nonlinear analysis, only simple modification is needed. First, ${}_0^{t+\Delta t}\mathbf{F}$ in Eq. (15) is divided into two parts as

$${}_0^{t+\Delta t}\mathbf{F} = {}_0^{t+\Delta t}\mathbf{F}^{\mathrm{structure}} + {}_0^{t+\Delta t}\mathbf{F}^{\mathrm{link}} \tag{27}$$

where ${}_0^{t+\Delta t}\mathbf{F}^{\mathrm{structure}}$ is simply the expression given by Eq. (15b) and ${}_0^{t+\Delta t}\mathbf{F}^{\mathrm{link}}$ denotes the contribution from elastic links. Since the elastic links behave linearly, we only have to replace Eq. (26a) by the following equation:

$$\left({}_0^t\mathbf{K}_{\mathrm{L}}^{(k-1)} + {}_0^t\mathbf{K}_{\mathrm{NL}}^{(k-1)} + \mathbf{K}^{\mathrm{link}}\right)\Delta\mathbf{U}^{(k)} = {}^{t+\Delta t}\mathbf{R} - {}_0^{t+\Delta t}\mathbf{F}^{(k-1)} \tag{28}$$

and use the remaining Eqs. (26b)–(26h) without being unchanged. It is noted again that the size of $\Delta\mathbf{U}^{(k)}$ in Eq. (28) is not the same as $\Delta\mathbf{U}^{(k)}$ in Eq. (26) because four nodes at every connections are assumed disconnected.

4.2. Nonlinear numerical analysis using the link approach

To show the superior behavior of the proposed link modeling approach over the convergence relaxation method by Pedersen et al. (2001) and Buhl et al. (2000), we consider the geometrical nonlinear analysis of the loaded structures shown in Fig. 14.

To solve the problem depicted in Fig. 14, we will consider three modeling techniques including the proposed link modeling technique, which is shown in Fig. 15. In Figs. 14 and 15, ω denotes the region occupied by the structure, and Ω, the square domain encompassing ω, can be viewed as the design domain if topology optimization is considered.

Obviously, the nonlinear analysis by the modeling shown in Fig. 15(a) will give the best result. The modeling technique in Fig. 15(b) has been used in the standard density-based SIMP topology optimization but often fails to yield converged solution unless the convergence criteria are relaxed (See Pedersen et al. (2001) and Buhl et al. (2000) for the details on the convergence relaxation scheme.); even if the convergence relaxation is employed, the incremental residual $\mathscr{R}^{(k)}$ (defined in Eq. (26h)) usually fluctuates as shown in Fig. 16(b). This fluctuation results from the fact that some low-stiffness elements (i.e., element with $E = 1.0 \times 10^{-9}$) have nonpositive-definite tangent stiffness matrices due to excessive deformations in the elements.

Since Modeling 2 and Modeling 3 can be directly applied to topology optimization problems, the performance of these two modeling techniques will be compared. Unlike Modeling 2, Modeling 3 (The proposed 6-DV link modeling technique) exhibits monotonic convergence behavior as shown in Fig. 16(c). Even if large displacements occur in some plane finite elements, large strain develops mainly in the link elements. Therefore, unless the original finite element discretization (i.e., such as the discretization by Modeling 1) has numerical problems, the present modeling technique does not cause numerical problems experienced by Modeling 2.

Now we compare the numbers of the Newton-Raphson iterations and the CPU times in Table 1. As manifested itself in Table 1, the present link modeling technique performs much better than Modeling 2. A few remarks on the modeling techniques may be needed in conjunction with topology optimization. When Modeling 3 is employed for topology optimization, the same finite element discretization can be used throughout the whole optimization process unlike in Modeling 2, and the numerical problems coming from low-density elements for nonlinear analysis can be avoided. We will show how this modeling technique works for topology optimization of geometrical nonlinear structures in the next section.

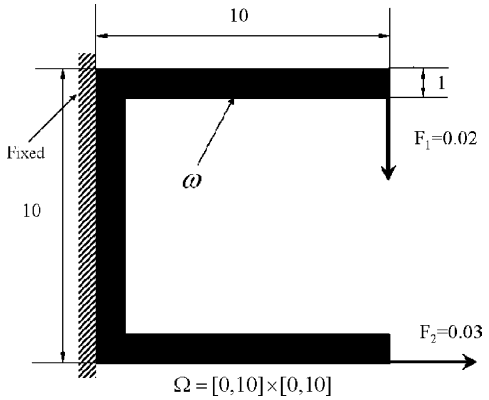

Fig. 14. A geometrical nonlinear structure ($E = 1$, $v = 0.3$) under two loads.

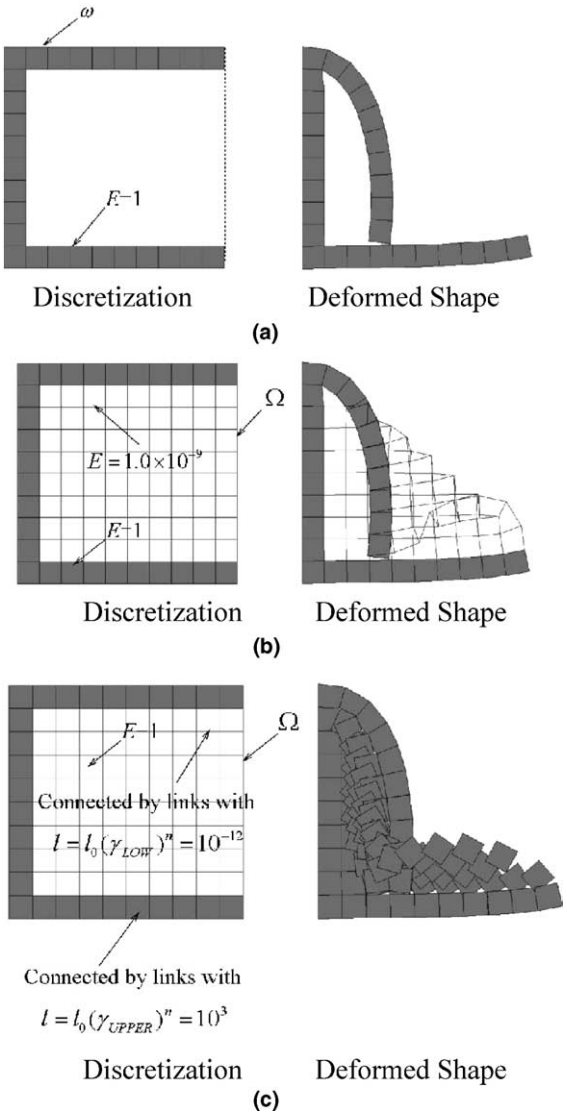

Fig. 15. Three modeling techniques and the deformed shapes: (a) Modeling 1 (only ω is discretized), (b) Modeling 2 (Ω is discretized where the nonstructural region is modeled by weak materials) and (c) Modeling 3 (Ω is discretized but only ω is connected by stiff links).

5. Element connectivity parameterization for nonliner problems

5.1. Topology optimization formulation using link modeling

The topology optimization for the compliance minimization of geometrically nonlinear structures can be written as

$$\underset{\gamma}{\text{Min}} \quad W(\gamma) = \mathbf{L}^{\mathrm{T}t+\Delta t}\mathbf{U}(\gamma) \tag{29a}$$

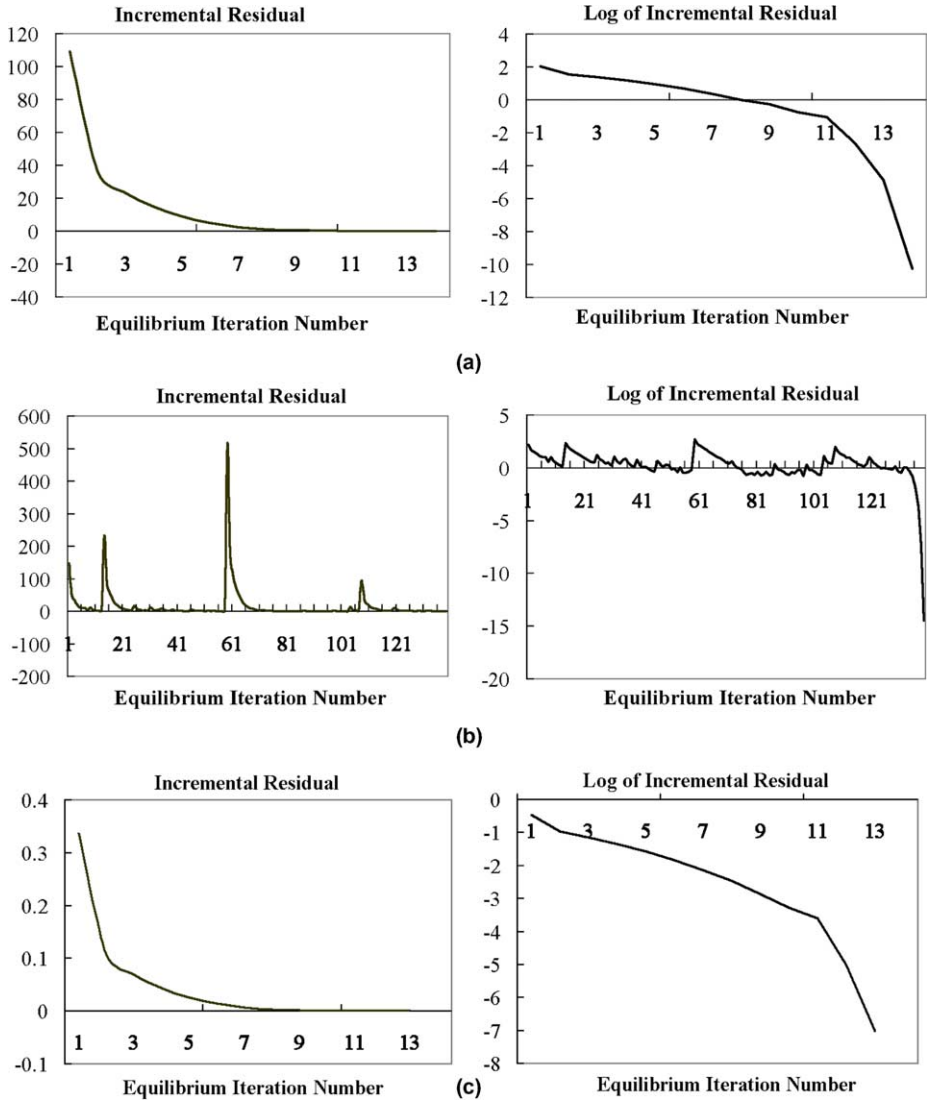

Fig. 16. The history of the incremental residual $\Re^{(k)}$ in the Newton–Raphson method for various modeling techniques: (a) Modeling 1, (b) Modeling 2, and (c) Modeling 3 (proposed link modeling).

Table 1
Comparison of the numerical results by three modeling techniques (convergence for $\|\mathscr{R}^{(k)}\| \leqslant 1.0 \times 10^{-7}$)

Modeling method	Displacement at loaded points		Newton–Raphson iterations	CPU time (s)
	F_1-loaded	F_2-loaded		
Modeling 1	(−6.013, 8.895)	(0.368, −0.532)	14	0.547
Modeling 2	(−6.013, 8.895)	(0.368, −0.532)	139	18.06
Modeling 3	(−6.013, 8.895)	(0.368, −0.532)	13	2.39

$$\text{subject to} \quad \sum_{e=1}^{N_p} \rho_e(\boldsymbol{\gamma}) v_e \leqslant V^* \tag{29b}$$

where the equilibrium condition Eq. (15a) is assumed to be satisfied. The time $t+\Delta t$ stands for the equilibrium state for a given load. In Eq. (29), $\mathbf{L}$ is a load vector consisting of zeros except for the positions where loads are applied, and ${}^{t+\Delta t}\mathbf{U}(\boldsymbol{\gamma})$ denotes the converged displacement of the geometrical nonlinear analysis.

To facilitate the calculation of $\partial W/\partial\gamma_i$, it is convenient to use the adjoint variables ${}^{t+\Delta t}\boldsymbol{\lambda}$ which satisfy

$${}^{t+\Delta t}\mathbf{K}_{\mathrm{T}}\,{}^{t+\Delta t}\boldsymbol{\lambda} = \mathbf{L} \tag{30}$$

where ${}^{t+\Delta t}\mathbf{K}_{\mathrm{T}}$ is the tangent stiffness matrix at the converged state $t+\Delta t$ of the geometrical nonlinear analysis. The definition of ${}^{t+\Delta t}\mathbf{K}_{\mathrm{T}}$ is

$${}^{t+\Delta t}\mathbf{K}_{\mathrm{T}} = -\left.\frac{\partial \mathscr{R}}{\partial \mathbf{U}}\right|_{\text{converged}} = \left({}_0{}^{t+\Delta t}\mathbf{K}_{\mathrm{L}} + {}_0{}^{t+\Delta t}\mathbf{K}_{\mathrm{NL}} + \mathbf{K}^{\text{link}}\right)\Big|_{\text{converged}} = \left({}^{t+\Delta t}\mathbf{K}^{\text{structure}} + \mathbf{K}^{\text{link}}\right)\Big|_{\text{converged}} \tag{31}$$

Now consider the following modified form of W for the sensitivity analysis:

$$W = \mathbf{L}^{\mathrm{T}}\,{}^{t+\Delta t}\mathbf{U}(\boldsymbol{\gamma}) + {}^{t+\Delta t}\boldsymbol{\lambda}\left({}^{t+\Delta t}\mathbf{R} - {}^{t+\Delta t}\mathbf{F}\right) \tag{32a}$$

$$\frac{\partial W}{\partial \gamma_i} = \mathbf{L}^{\mathrm{T}}\left(\frac{\partial\,{}^{t+\Delta t}\mathbf{U}(\boldsymbol{\gamma})}{\partial \gamma_i}\right) + {}^{t+\Delta t}\boldsymbol{\lambda}^{\mathrm{T}}\left(\frac{\partial\,{}^{t+\Delta t}\mathbf{R}}{\partial \gamma_i} - \frac{\partial\,{}^{t+\Delta t}\mathbf{F}^{\text{structure}}}{\partial \gamma_i} - \frac{\partial\,{}^{t+\Delta t}\mathbf{F}^{\text{link}}}{\partial \gamma_i}\right) \tag{32b}$$

$$\frac{\partial\,{}^{t+\Delta t}\mathbf{F}^{\text{structure}}}{\partial \gamma_i} = \frac{\partial\,{}^{t+\Delta t}\mathbf{F}^{\text{structure}}}{\partial\,{}^{t+\Delta t}\mathbf{U}}\frac{\partial\,{}^{t+\Delta t}\mathbf{U}}{\partial \gamma_i} = {}^{t+\Delta t}\mathbf{K}_{\mathrm{T}}^{\text{structure}}\frac{\partial\,{}^{t+\Delta t}\mathbf{U}}{\partial \gamma_i} \tag{32c}$$

$$\begin{aligned}\frac{\partial\,{}^{t+\Delta t}\mathbf{F}^{\text{link}}}{\partial \gamma_i} &= \frac{\partial}{\partial \gamma_i}\left[\mathbf{K}^{\text{link}}(\boldsymbol{\gamma})\,{}^{t+\Delta t}\mathbf{U}(\boldsymbol{\gamma})\right] = \mathbf{K}^{\text{link}}(\boldsymbol{\gamma})\frac{\partial\,{}^{t+\Delta t}\mathbf{U}(\boldsymbol{\gamma})}{\partial \gamma_i} + \frac{\partial \mathbf{K}^{\text{link}}(\boldsymbol{\gamma})}{\partial \gamma_i}\,{}^{t+\Delta t}\mathbf{U}(\boldsymbol{\gamma}) \\ &= \mathbf{K}^{\text{link}}(\boldsymbol{\gamma})\frac{\partial\,{}^{t+\Delta t}\mathbf{U}(\boldsymbol{\gamma})}{\partial \gamma_i} + \frac{\mathrm{d}k_i^{\text{link}}(\gamma_i)}{\mathrm{d}\gamma_i}\,{}^{t+\Delta t}u_i(\boldsymbol{\gamma})\end{aligned} \tag{32d}$$

where ${}^{t+\Delta t}u_i$ denotes the displacements of nodes at connection i. Substituting Eq. (32c,d) and $\partial\,{}^{t+\Delta t}\mathbf{R}/\partial\gamma_i = 0$ into Eq. (32b) yields

$$\frac{\partial W}{\partial \gamma_i} = \left(\mathbf{L}^{\mathrm{T}} - {}^{t+\Delta t}\boldsymbol{\lambda}^{\mathrm{T}}\,{}^{t+\Delta t}\mathbf{K}_{\mathrm{T}}\right)\left(\frac{\partial\,{}^{t+\Delta t}\mathbf{U}(\boldsymbol{\gamma})}{\partial \gamma_i}\right) - {}^{t+\Delta t}\lambda_i^{\mathrm{T}}\frac{\mathrm{d}k_i^{\text{link}}}{\mathrm{d}\gamma_i}\,{}^{t+\Delta t}u_i(\boldsymbol{\gamma}) = -{}^{t+\Delta t}\lambda_j^{\mathrm{T}}\frac{\mathrm{d}k_i^{\text{link}}}{\mathrm{d}\gamma_i}\,{}^{t+\Delta t}u_j(\boldsymbol{\gamma}) \tag{33}$$

The validity of the sensitivity expression in Eq. (33) has been confirmed by comparing the result by Eq. (33) and the result by the finite difference scheme. As can be seen in Eq. (33), the sensitivity $\partial W/\partial\gamma_i$ is explicitly affected by the stiffness of the links at connection i.

5.2. Numerical studies

A few benchmark topology optimization problems requiring geometrical nonlinear analyses will be solved by using the present element connectivity parameterization method. As optimization algorithms, the optimality criteria method is used for compliance minimization and the method of moving asymptotes by Svanberg (1987) is used for compliant mechanism and multiphysics problems. Since there are many local optimal points in the topology optimization problems, different initial guesses could produce different local optima (see Pedersen et al., 2001). In the present investigations, uniform values of $\boldsymbol{\gamma}$ that satisfy a given mass constraints are used unless stated otherwise.

Case 1: Compliance minimization for a center-loaded structure

We begin with the compliance minimization depicted in Fig. 17(a). This problem was worked out by Buhl et al. (2000) and is perhaps one of difficult problems to solve with the standard SIMP formulation. We use exactly the same numerical data that were used by Buhl et al. (2000).

The results shown in Fig. 18(a) and (b) are obtained only with 15 and 21 optimization iterations. Compared with 600 iterations in Buhl et al. (2000), the present method requires much less number of optimiza-

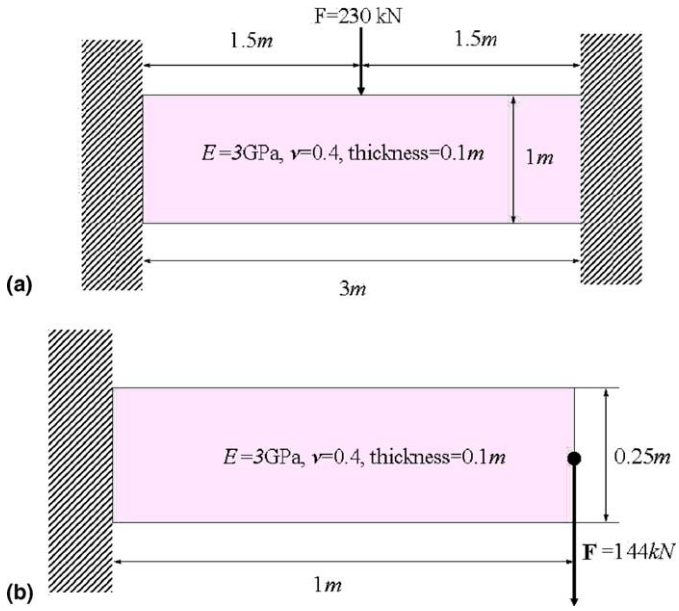

Fig. 17. Problem definition of the compliance minimization of geometrically nonlinear structures: (a) Case 1: mass constraint ratio=10%, domain discretized by 120×40 4-node bilinear finite elements, (b) Case 2: mass constraint ratio=50%, domain discretized by 80×20 4-node bilinear finite elements.

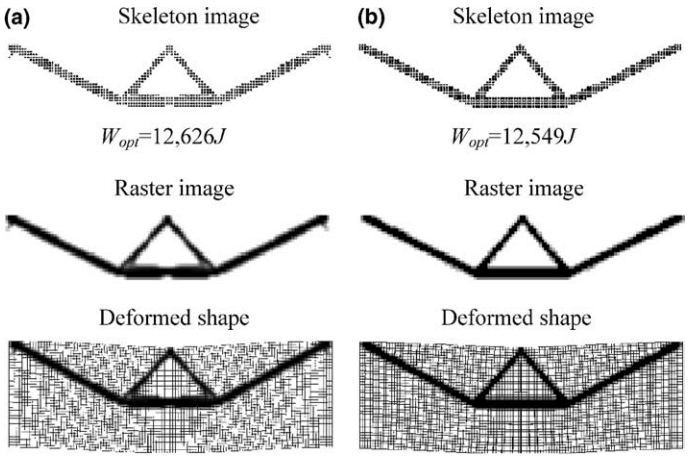

Fig. 18. The optimized results obtained by the proposed element connectivity parameterization scheme for the problem depicted in Fig. 17(a). (a) Without filtering, and (b) with filtering.

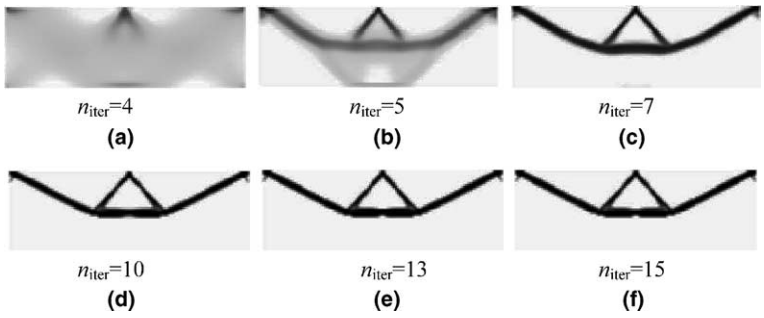

Fig. 19. The raster image obtained by the proposed method without filtering at various iteration steps (n_{iter}: the iteration number).

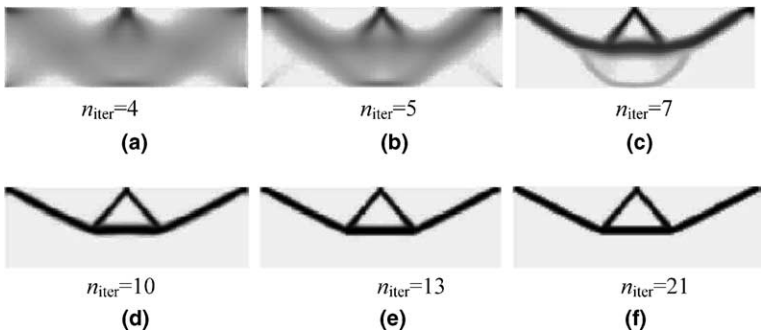

Fig. 20. The raster image obtained by the proposed method with filtering at various iteration steps (n_{iter}: the iteration number).

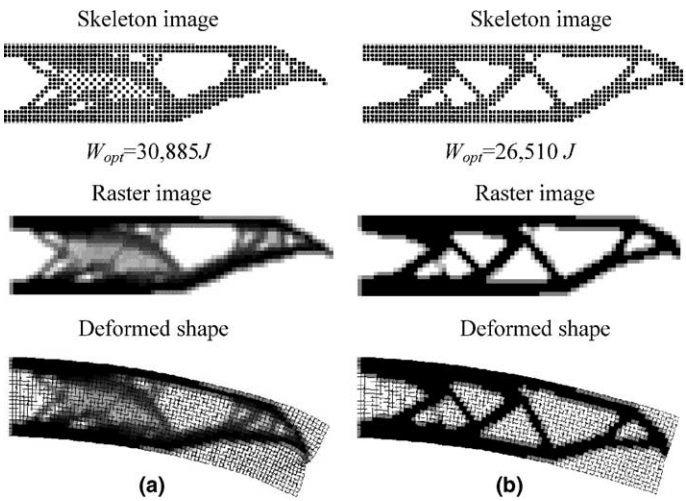

Fig. 21. The optimized results obtained by the proposed element connectivity parameterization scheme for the problem depicted in Fig. 17(b). (a) Without filtering, and (b) with filtering.

tion iterations and the optimized values W_{opt} are comparable with those given in Buhl et al. (2000). The main reason for the substantial reduction in the iteration number is that no unstable element occurs in

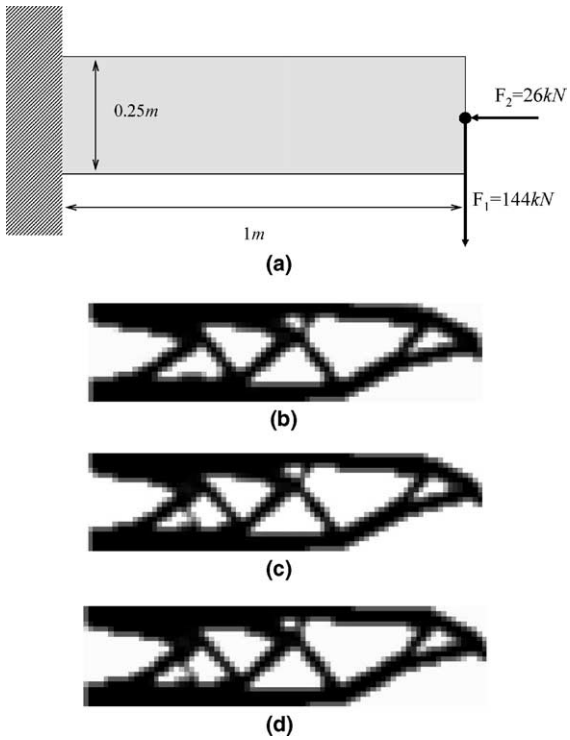

Fig. 22. The effect of the additional consideration of the horizontal force in the end compliance minimization problem. (a) Problem definition. The results for the weighting factors (c_1 and c_2) equal to (b) (0.25, 0.75), (c) (0.5, 0.5), and (d) (0.75, 0.25).

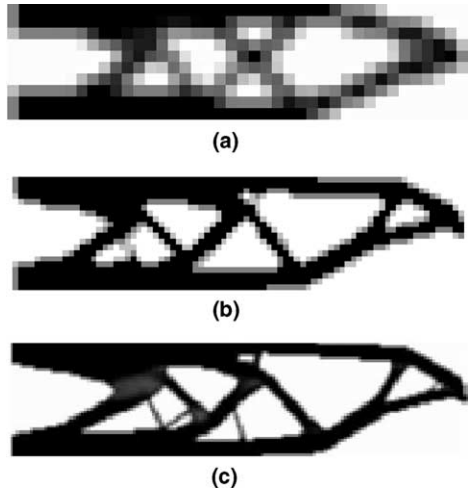

Fig. 23. The results with the various meshes with the discretization of: (a) 40×10, (b) 80×20, and (c) 160×40.

the proposed modeling scheme due to zero-length elastic links. Though it was difficult to compare directly the CPU times by the present method and the method used in Buhl et al. (2000), the present method requires a very small number of optimization iterations and takes short CPU time for a typical geometrical nonlinear analysis (as seen in Table 1). Figs. 19 and 20 show the raster images obtained by the present approach with and without filtering. These figures show that meaningful raster images appear even after the first few iterations.

Case 2: Compliance minimization for an end-loaded problem

As the second case study, the end compliance minimization problem described in Fig. 17(b) is considered. Although only a vertical tip load should be considered, two loads both in the vertical and horizontal directions were considered in the existing literature to obtain physically meaningful results.

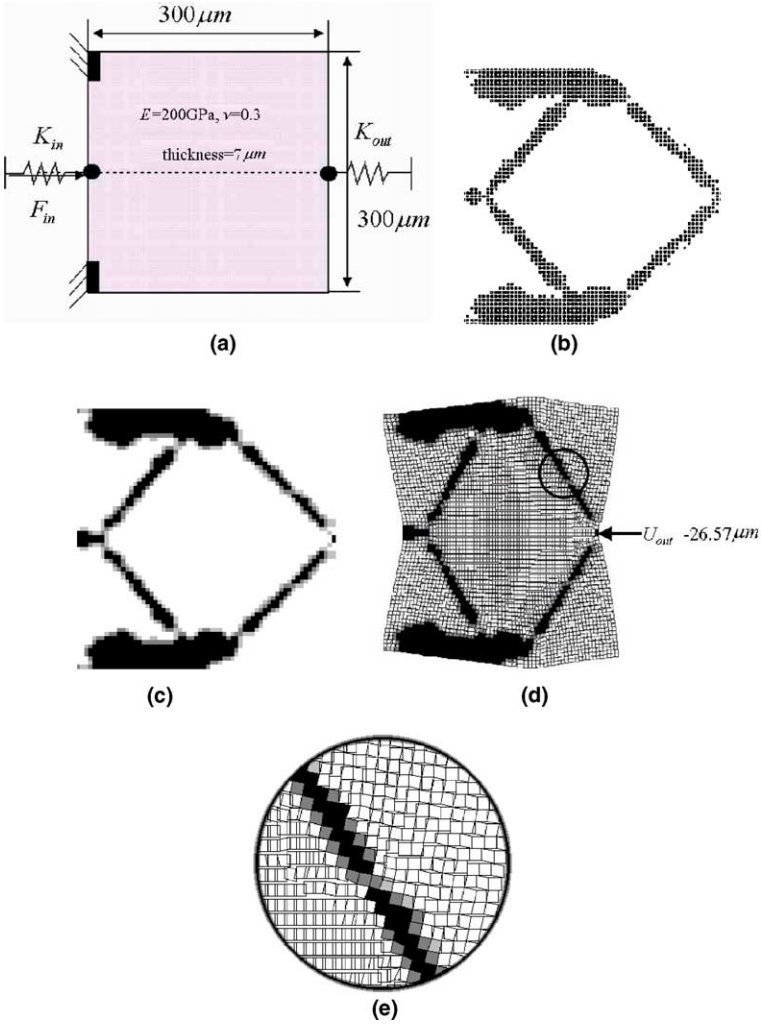

Fig. 24. The displacement inverter topology optimization and the optimized results by the present method after filtering: (a) problem definition ($K_{in} = 100\,N/m$, $K_{out} = 400\,N/m$, $F_{in} = 2\,mN$, mass constraint = 30%), (b) the skeleton image, (c) raster image, (d) the deformed shape, and (e) zoomed view of the encircled region in (d).

When the present formulation is employed, however, one does not need to consider the artificial horizontal load to obtain meaningful results. The optimized results by the present approach are shown in Fig. 21. Without using any convergence relaxation or similar treatments, the present method yields satisfactory results. Nevertheless, it will be interesting to consider the effect of the artificial horizontal force on the optimal topologies when the present ECP formulation is employed. Fig. 22(a) describes the problem considered at Fig. 22(b) through Fig. 22(d). The objective function W in this case is treated as the function for a multiload case where W is replaced by $W_{\text{multi}} = c_1 W_{\text{F}_1} + c_2 W_{\text{F}_2}$ (c_i: weighting factor). The symbol W_{F_i} is the compliance upon the force F_i shown in Fig. 22. The effects of meshes on the optimized results are shown in Fig. 23.

Case 3: Compliance mechanism problem

The displacement inverter design problem, which is one of the typical compliant mechanism design problems, is considered, and the design problem is depicted in Fig. 24(a). A linear version of this problem was also solved by Yoon et al. (2004) but the results shown in Fig. 24(b)–(e) are obtained with the consideration of geometrical nonlinear behavior.

In obtaining the results shown in Fig. 24(b)–(e) by the proposed link-based approach, no numerical instability resulting from the nonpositive-definiteness of the low-density elements is encountered at all. Since we use the 4-node bilinear finite element, the filtering scheme alone cannot avoid the presence of the one-point hinge. If one-point hinge controlling methods that are developed by Poulsen (2003) and Yoon et al. (2004) are employed, hingeless designs may be obtained. However, the application of the hinge-controlled technique has not been yet incorporated with the present topology optimization formulation.

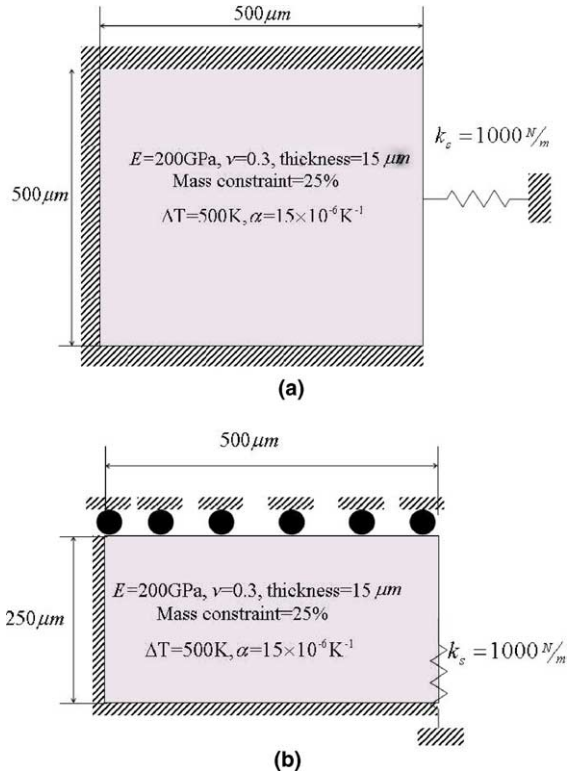

Fig. 25. The problem definition of the thermal actuator design. (a) Case 4 and (b) Case 5.

It should be noted again that the grey and white regions shown in Fig. 24(d) and (e) have appeared only in the raster image, not during the numerical analysis stage.

Cases 4 and 5: Thermal actuator design problems

As Cases 4 and 5, we consider the topology optimization of thermal actuators where elastic deformations are geometrically nonlinear by Sigmund (2001). The problem definitions for Case 4 and Case 5 are given in

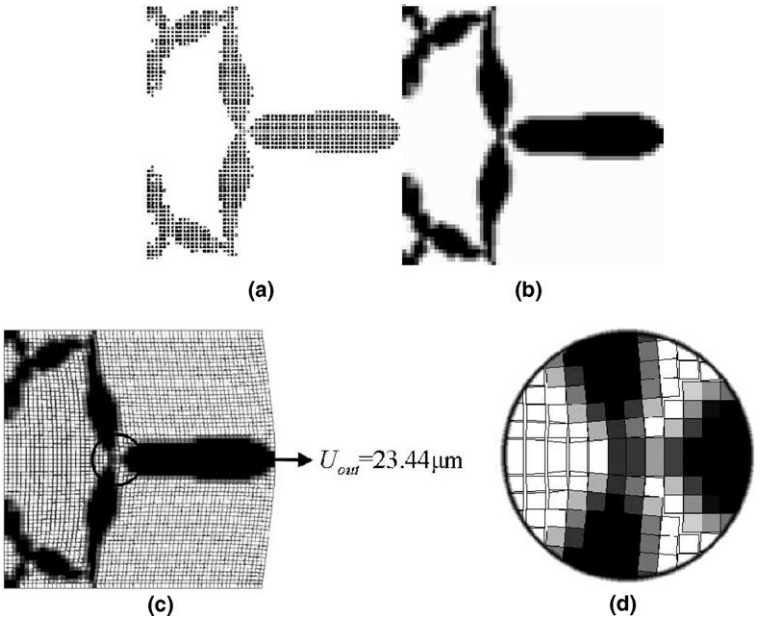

Fig. 26. The optimized result by the present method for Case 4 defined in Fig. 25(a): (a) skeleton image, (b) raster image, (c) deformed shape and (d) zoomed view of the encircled region in (c).

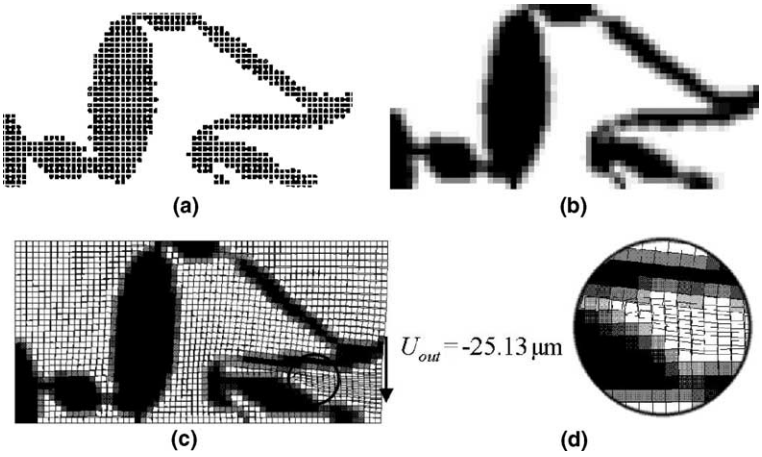

Fig. 27. The optimized result by the present method for Case 5 defined in Fig. 25(b). (a) Skeleton image, (b) raster image, (c) deformed shape and (d) zoomed view of the encircled region in (c).

Fig. 25(a) and (b), respectively. In Fig. 25, the thermal expansion coefficient is denoted by α, and the uniform heating of $\Delta T = 500\,\mathrm{K}$ is assumed.

For the thermal actuator design problems, we use the following constitutive relation:

$$ {}_0^{t+\Delta t}S_{ij} = \mathbf{C}({}_0^{t+\Delta t}\epsilon_{ij} - \alpha\Delta\mathbf{T}) \tag{34} $$

The optimized results by the present method for Case 4 and Case 5 are shown in Figs. 26 and 27, respectively. For Case 4, only the half of the design domain is discretized due to the symmetry, but the result is given in the full scale. As in the previous cases, no convergence problem occurs when the proposed formulation is employed for topology optimization involving geometrically nonlinear analysis.

6. Concluding remarks

A new formulation for topology optimization of geometrically nonlinear structures is presented. To avoid the numerical instability of low-stiffness finite elements appearing in the standard element density-based SIMP formulation, topology optimization is reformulated as the problem to find the optimal inter-element connectivity distribution while the finite elements discretizing the design domain are made to have the stiffness of real materials throughout the optimization process. The following is the summary of the findings through this investigation.

1. The introduction of elastic links was very effective in representing the degree of inter-element connectivity.
2. Both linear and nonlinear responses of structures were accurately predicted. Subsequently, physically meaningful optimal results were found without artificial numerical treatments. The suggested value of the link stiffness l_0 is $(100 \sim 1000)Eh$, where E is Young's modulus and h is the size of plane finite elements.
3. By the link-based modeling, low-stiffness links also appear but do not cause any instability problems because they are one-dimensional structural elements.
4. Since no numerical instability problem occurs during topology optimization by the present element connectivity parameterization method, the initial design domain discretization can be used throughout the whole optimization process.
5. The total number of degrees of freedom for numerical analysis increases almost four times in two-dimensional problems. Therefore, the proposed method in the linear structural problems is not as efficient as the SIMP method. However, the present method substantially reduces the CPU time for the Newton–Raphson iterative procedure and also takes much smaller optimization iterations. Therefore, the total solution speedup for geometrically nonlinear problems is significant.
6. For benchmark design problems involving geometrically nonlinear analysis, the present method has performed well.
7. Regardless of the introduction of the elastic links, the overall solution behavior is controlled by the finite element mesh used to discretize the design domain; for instance, checkerboard patterns appear when 4-node bilinear finite elements are used. However, checkerboard pattern formation and similar problems can be controlled by existing techniques such as the filtering technique.
8. Though the proposed zero-length elastic link modeling technique was primarily devised to deal with the topology optimization involving geometrical nonlinear behavior, the technique is expected to be also useful for other classes of topology optimization problems.

References

Bathe, K.J., 1996. Finite Element Procedures. Prentice-Hall, New Jersey.

Belytschko, T., Liu, W.K., Moran, B., 2000. Nonlinar Finite Elements for Continua and Structures. John Wiley & sons, New York.

Bendsøe, M.P., Kikuchi, N., 1988. Generating optimal topologies in structural design using a homogenization method. Comput. Meth. Appl. Mech. Engng. 71, 197–224.

Bendsøe, M.P., Sigmund, O., 2003. Topology Optimization Theory, Methods and Applications. Springer-Verlag, New York.

Bruns, T.E., Tortorelli, D.A., 2001. Topology optimization of nonlinear elastic structures and compliant mechanisms. Comput. Method Appl. Mech. Engng. 190 (26–27), 3443–3459.

Bruns, T.E., Tortorelli, D.A., 2003. An element removal and reintroduction strategy for the topology optimization of structures and compliant mechanisms. Int. J. Num. Methods Engng. 57, 1413–1430.

Buhl, T., Pedersen, C.B.W., Sigmund, O., 2000. Stiffness design of geometrically nonlinear structures using topology optimization. Struct. Multidiscip. Optimizat. 19 (2), 93–104.

Chang, D.C., 1974. Effects of flexible connections on body structural response. SAE Transactions 83, 233–244.

Cho, S.H., Jung, H.S., 2003. Design sensitivity analysis and topology optimization of displacement-loaded nonlinear structures. Comput. Methods Appl. Mech. Engng. 192, 2539–2553.

Gea, H.C., Luo, J., 2001. Topology optimization of structures with geometrical nonlinearities. Comput. Struct. 79, 1977–1985.

Kim, Y.Y., Yim, H.J., Kang, J.H., Kim, J.H., 1995. Reconsideration of the joint modeling technique in a box-beam T-joint. SAE 951108, 275–279.

Kobayashi, S., Oh, S.I., Altan, T., 1989. Metal Forming and The Finite-Element Method. Oxford University Press, New York.

Pedersen, C.B.W., Buhl, T., Sigmund, O., 2001. Topology synthesis of large-displacement compliant mechanisms. Int. J. Num. Methods Engng. 50, 2683–2705.

Poulsen, T.A., 2003. A new scheme for imposing a minimum length scale in topology optimization. Int. J. Num. Methods Engng. 57, 741–760.

Sigmund, O., Petersson, J., 1998. Numerical instabilities in topology optimization: a survey on procedures dealing with checkerboards, mesh-dependencies and local minima. Struct. Optimizat. 16, 68–75.

Sigmund, O., 2001. Design of Multiphysics actuators using topology optimization–Part I: One material Structure. Comput. Meth. Appl. Mech. Eng. 190 (49–50), 6577–6604.

Suzuki, K., 2003. University of Tokyo, Private communication.

Svanberg, K., 1987. The method of moving asymptotes—a new method for structural optimization. Int. J. Num. Methods Engng. 24, 359–373.

Yoon, G.H., Kim, Y.Y., Bendsøe, M.P., Sigmund, O., 2004. Hinge-free topology optimization with embedded translation-invariant differentiable wavelet shrinkage. Structural Multidisciplinary Optimization 27 (3), 139–150.